sustainability

MDPI

Article

Analysis of Electrochemical Properties of LT-SOFCs According to Thickness of PrO_x Cathode Interlayer

Ji-Woong Jeon [1], Jun-Geon Park [1], Geon-Hyeop Kim [1], Seung-Heon Lee [1], Jeong-Woo Shin [2,*] and Gu-Young Cho [1,*]

[1] Department of Mechanical Engineering, Dankook University, 152 Jukjeon-ro, Suji-gu, Yongin-si 16890, Republic of Korea; zwesl@dankook.ac.kr (J.-W.J.); 32191827@dankook.ac.kr (J.-G.P.); 32190315@dankook.ac.kr (G.-H.K.); d72240134@dankook.ac.kr (S.-H.L.)

[2] School of Mechanical & Aerospace Engineering, Nanyang Technological University, 50 Nanyang Avenue, Singapore 639798, Singapore

* Correspondence: jeongwoo.shin@ntu.edu.sg (J.-W.S.); guyoungcho@dankook.ac.kr (G.-Y.C.)

Abstract: Solid oxide fuel cells (SOFCs) are attracting attention as an eco-friendly power source because they show high power density. However, SOFC requires a high-temperature environment of 800 °C or higher, and accordingly, the problem of thermal stability of the material constituting SOFC has been raised. On the other hand, low-temperature solid oxide fuel cells (LT-SOFCs) research is steadily progressing to improve the electrochemical performance at low temperatures by improving the oxygen reduction reaction of the cathode by applying a cathode interlayer of various materials. In this study, LT-SOFCs were manufactured and electrochemically evaluated using praseodymium oxide (PrO_x) as a cathode interlayer. Scandium Stabilized Zirconia (ScSZ) pellets were used as electrolyte support for LT-SOFC, and PrO_x was deposited by various thicknesses as a cathode interlayer on ScSZ pellets by a sputtering process. Pt and Ni were deposited under the same process conditions for the cathode and anode, respectively. To analyze the thin-film characteristics of the PrO_x cathode interlayer, SEM (Scanning Electron Microscopy), X-ray Diffraction (XRD), and XPS (X-ray Photoelectron Spectroscopy) were analyzed. The electrochemical characteristics of LT-SOFCs were evaluated by electrochemical impedance spectroscopy (EIS). Hydrogen was supplied to the anode at the flow rate of 50 sccm, and the performance of LT-SOFC was evaluated at 500 °C by exposing the cathode to the atmosphere.

Keywords: solid oxide fuel cell; cathode interlayer; praseodymium oxide; reactive sputtering; electrochemical impedance spectroscopy

Academic Editor: Nicu Bizon

Received: 10 December 2024
Revised: 3 February 2025
Accepted: 5 February 2025
Published: 8 February 2025

Citation: Jeon, J.-W.; Park, J.-G.; Kim, G.-H.; Lee, S.-H.; Shin, J.-W.; Cho, G.-Y. Analysis of Electrochemical Properties of LT-SOFCs According to Thickness of PrO_x Cathode Interlayer. *Sustainability* **2025**, *17*, 1403. https://doi.org/10.3390/su17041403

1. Introduction

Due to recent climate changes, the concepts of eco-friendliness and sustainable development have become increasingly prominent. Therefore, research on eco-friendly power sources that can replace conventional internal combustion engines has intensified. In particular, Solid Oxide Fuel Cells (SOFCs) are gaining attention as eco-friendly power sources due to their excellent efficiency [1–8]. Generally, SOFCs require high operating temperatures, typically above 800 °C, because the ionic conductivity of the electrolyte is very low at lower temperatures [1,9–11]. However, the high-temperature operating conditions raise concerns about the thermal stability of SOFCs. Therefore, research is consistently being conducted to reduce operating temperatures for thermal stability and to prevent performance degradation during low-temperature operation [12–14].

Among the various methods to improve the electrochemical performance of low-temperature SOFCs (LT-SOFCs). Representative examples include previous studies on composite cathode fabrication that improved electrochemical properties [15,16]. Alternatively, the reaction of the cathode can be enhanced by applying a very thin capping layer to its surface [17,18]. However, these methods have the drawback of complexity in optimizing the fabrication process. Meanwhile, one of the relatively simple methods to improve the electrochemical performance of LT-SOFC cathodes is the use of a cathode interlayer [19–21]. Applying a cathode interlayer optimizes the cathode nanostructure, reducing resistance as oxygen ions (O^{2-}) move from the cathode to the electrolyte, facilitating electrochemical reactions more effectively [22]. Additionally, it promotes the oxygen reduction reaction, enhancing catalytic activity even at relatively low temperatures [23]. According to the study by Lee et al., the performance of LT-SOFCs was improved by applying Gadolinia doped ceria (Gd_2O_3, GDC) as a cathode interlayer to reduce the activation energy of the ORR reaction at the interface between the cathode and the electrolyte [24]. Not only does it suppress secondary phases, but it also has many advantages as a cathode interlayer due to its ease of fabrication using various manufacturing methods such as wet-chemical methods, CVD, and ALD [25,26]. In a previous study by Sumi. H., an LDC intermediate layer was applied between the YSZ electrolyte and the LSCF cathode, which significantly improved electrochemical performance due to its excellent oxygen ion conductivity and high oxygen storage capacity [27]. Furthermore, prior research has improved performance by reducing the polarization loss with the application of SDC interlayer [28].

Praseodymium oxide (PrO_x) is a rare earth oxide containing a mixed state of Pr ions with various oxidation states, such as Pr^{3+} and Pr^{4+} [29,30]. PrO_x is characterized by oxygen vacancies, which enhance its catalytic activity [16,31]. In PrO_x, Pr^{3+} promotes the formation of oxygen vacancies, thereby enhancing oxygen ion conductivity. Additionally, Pr^{4+} increases reversible redox activity, improving catalytic performance [32,33]. According to previous studies, PrO_x was applied to the cathode using the wet-chemical infiltration method to improve the charge transfer process of the existing cathode, thereby enhancing the electrochemical performance of SOFCs [34]. Furthermore, according to the study by Satoshi Okada et al., a symmetric cell was fabricated using PrO_x through a thin-film process, followed by surface modification with $BaPrO_3$ on both electrodes, after which electrochemical evaluations were conducted [35].

Meanwhile, powder-based fabrication methods, such as tape casting and infiltration, are widely used as fabrication techniques for manufacturing components of LT-SOFCs [34,36–40]. However, such powder processes have difficulty achieving uniform thin-film formation and precise nanoscale control [10,41]. Among these methods, the sputtering process is a physical vapor deposition technique that forms thin films by bombarding a target material with ions under high vacuum conditions [4,24]. Through the sputtering process, components of LT-SOFCs, including electrodes, can be fabricated at the nanoscale, and the microstructure can be controlled by adjusting temperature and pressure conditions [42,43]. The sputtering process not only enables mass production but also allows for the formation of uniform thin films. By optimizing the structure and thickness of the thin films, it enhances electrochemical performance [24,41].

However, research on the fabrication of PrO_x interlayers using thin-film processes and their application in LT-SOFCs remains limited. In this study, PrO_x is fabricated as a cathode interlayer using a thin-film process for LT-SOFCs. Furthermore, the electrochemical performance is evaluated based on the thickness of the cathode interlayer to determine the optimal thickness.

2. Experiments

The fabrication process of the PrO_x cathode interlayer was conducted using RF sputtering, as illustrated in Figure 1 (KVS-2000L, Korea Vacuum Tech, Gimpo-si, Republic of Korea). A silicon wafer was used as the deposition substrate to analyze the physical and chemical properties of PrO_x. For the PrO_x deposition process, a 2-inch diameter Pr_6O_{11} target was used (VTM, Incheon, Republic of Korea). Additionally, reactive sputtering was utilized during the sputtering process to ensure stable deposition of Pr_6O_{11} [35,44]. To fabricate dense PrO_x thin films, the process pressure was uniformly set to 5 mTorr. For reactive sputtering, Ar and oxygen were supplied at 24 sccm and 6 sccm, respectively. The substrate rotated at 20 rpm, and PrO_x thin films of varying thicknesses were deposited based on deposition time. To analyze the thickness of the PrO_x films, Scanning Electron Microscopy (SEM, S-5200, Hitachi, Tokyo, Japan) was used. In addition, annealed for 1 h, and as-deposited PrO_x thin films were produced at 500 °C to analyze the crystal structure change caused by the operating temperature of LT-SOFCs. X-ray Diffraction (XRD, SmartLab, Rigaku, Tokyo, Japan) analysis was performed to analyze the crystallinity of the thin film. In addition, X-ray Photoelectron Spectroscopy (XPS, AXIS Supra+, Kratos, Manchester, UK) was performed to analyze the chemical composition of PrO_x.

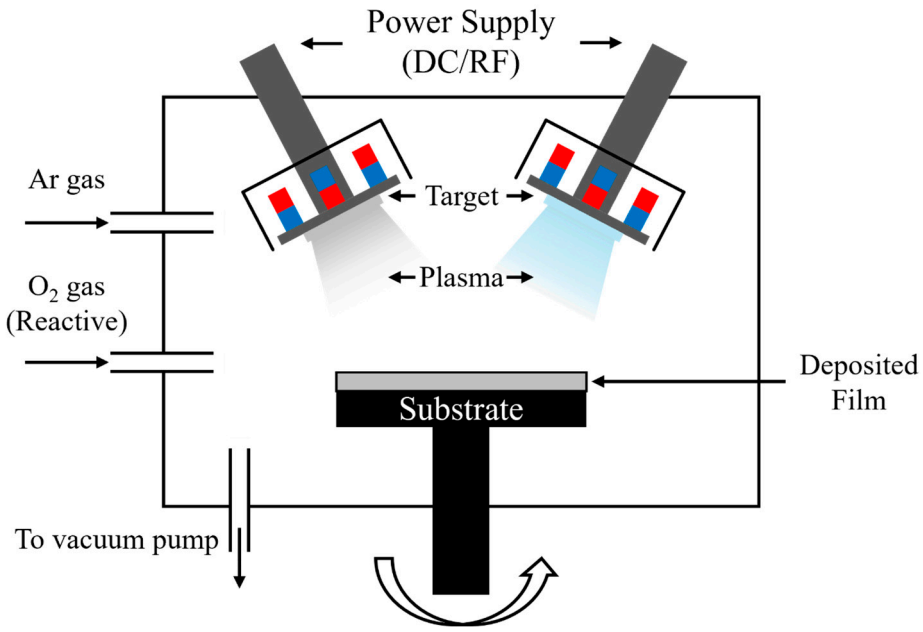

Figure 1. Schematic diagram of DC/RF magnetron sputtering system.

As shown in Figure 2, LT-SOFCs with a reaction area of 1.5 mm^2 were fabricated. Sc_2O_3-stabilized zirconia (ScSZ) pellets were used as electrolyte support. ScSZ is known for its high oxygen ion conductivity and excellent thermal stability [45]. As shown in Table 1, The PrO_x cathode interlayer was deposited on ScSZ pellets with thicknesses of 30 nm, 55 nm, and 150 nm under the same conditions as those used for deposition on Si wafers. Pt has very high catalytic activity against oxygen reduction reaction (ORR) [1]. Therefore, as shown in Table 2, the cathode was deposited using a Pt target (VTM, Incheon, Republic of Korea) at 50 mTorr with a supply of 30 sccm Ar gas at 100 W [46,47]. Similarly, the anode was deposited using a Ni target (VTM, Incheon, Republic of Korea) at 30 mTorr with a 30 sccm Ar gas supply at 100 W. Ni has very high catalytic activity in the hydrogen oxidation reaction and has excellent electron conductivity, enabling efficient movement of electrons from the anode [48].

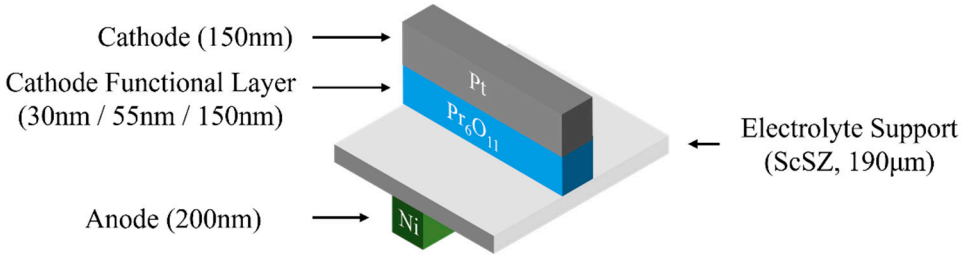

Figure 2. Schematic diagram of LT-SOFCs.

Table 1. Experimental parameters of PrO_x thin-film fabrication.

Parameters	Pr30	Pr55	Pr150
Thickness	30 nm	55 nm	150 nm
Pressure		5 mTorr	
Gas Flow		Ar 24 sccm + O_2 6 sccm	
Deposition Power		40 W	
Temperature		Room Temperature	

Table 2. Experimental parameters of electrode fabrication.

Parameters	Pt (Cathode)	Ni (Anode)
Thickness	150 nm	200 nm
Pressure	50 mTorr	30 mTorr
Gas Flow	Ar 30 sccm	
Deposition Power	100 W	
Temperature	Room Temperature	

To analyze the electrochemical properties of LT-SOFCs with interlayers of varying thickness, a custom-made SOFC test station, as shown in Figure 3, was utilized. The anode and cathode were connected using Ag wire and Ag paste (Silver Conductive Ink Liquid S-020, Alfa Aesar, Haverhill, MA, USA). Ceramic sealant (Ceramabond 571, Aremco, Valley Cottage, NY, USA) was used for sealing. LT-SOFC tests were conducted at 500 °C. Hydrogen gas (H_2) was supplied at a flow rate of 50 sccm at 1.2 bar, while the cathode was exposed to ambient air. Electrochemical properties were measured using potentiostats (SP-300, Biologic, Seyssinet-Pariset, France). After performance measurements, electrochemical impedance spectroscopy (EIS) was performed by applying an alternating current perturbation of 10 mV at 0.5 V over a frequency range of 1 Hz to 1 MHz.

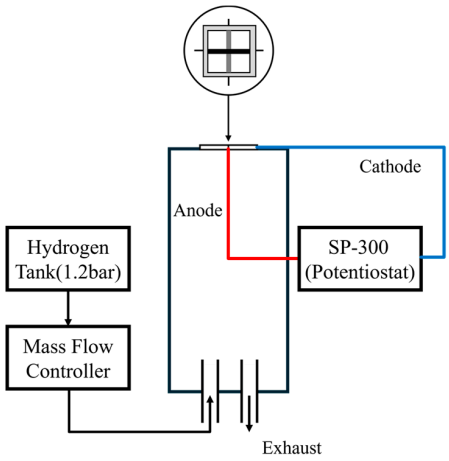

Figure 3. Schematic diagram of custom-made LT-SOFCs system.

3. Results and Discussion

3.1. Properties of PrO_x Thin Films

Figure 4 shows the surface of PrO_x thin films deposited with various thicknesses on a Si wafer. All films were observed to be deposited in a dense form. However, as the thickness of the PrO_x thin film decreased, a trend of decreasing grain size was observed. This trend of smaller grain sizes in thinner films is consistent with previous studies [43,49,50]. The decrease in grain size results in a relatively larger number of grain boundaries, which increases the likelihood of resistance during oxygen ion movement compared to larger grain sizes [51,52].

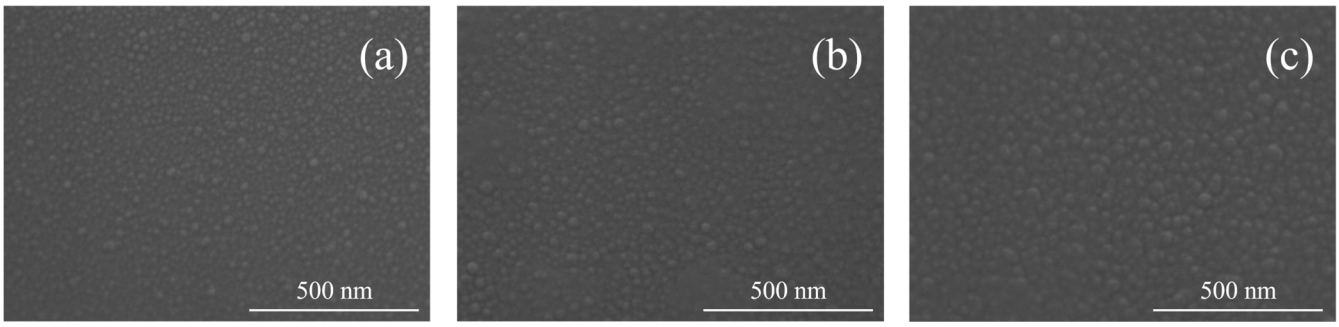

Figure 4. Surface images of PrO_x thin films on Si wafer measured by SEM image (**a**) Pr30, (**b**) Pr55, and (**c**) Pr150.

Figure 5 shows the cross-sections of PrO_x thin films with various thicknesses deposited on a Si wafer, along with the Pt thin films deposited on top of them. In Figure 5a, the PrO_x thickness is approximately 30 nm; in Figure 5b, it is about 55 nm; and in Figure 5c, it is approximately 150 nm. The Pt layer in all samples showed a uniform thickness of approximately 150 nm. According to numerous previous studies, an increase in the thickness of the cathode interlayer tends to elongate the conduction path, leading to a decrease in oxygen ion conductivity. Consequently, this leads to an increase in ohmic resistance in LT-SOFCs [1].

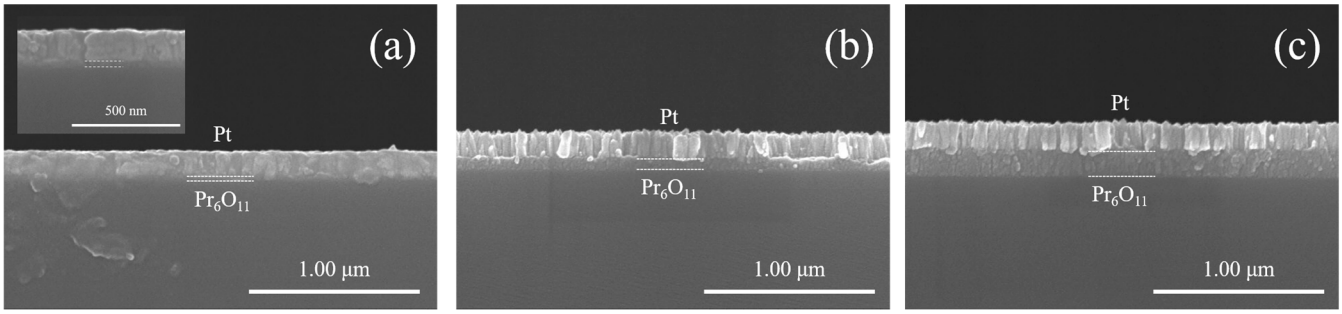

Figure 5. Cross-sectional images of PrO_x thin films on Si wafer measured by SEM image (**a**) Pr30, (**b**) Pr55, and (**c**) Pr150.

Pr_6O_{11} has a crystal structure based on a fluorite structure. Notably, it exhibits a mixed state of Pr^{3+} and Pr^{4+}, which leads to the formation of oxygen vacancies, resulting in a defective-fluorite structure [44]. As shown in Figure 6, XRD analysis revealed that peaks were observed at (111), (200), (220), and (311) planes both in the as-deposited state and after annealing at 500 °C for 1 h. The XRD analysis confirmed that the peak positions remained the same before and after heat treatment, indicating that no phase change occurred in the material [29]. Meanwhile, in the case of annealing at 500 °C, sharper peaks were observed compared to the as-deposited state. This indicates that crystallinity improved with heat

treatment at 500 °C. At the operating temperature of LT-SOFCs, this suggests reduced internal defects and micro strains, enhancing lattice stability and increasing pathways of ion conduction, thereby improving electrochemical performance [53].

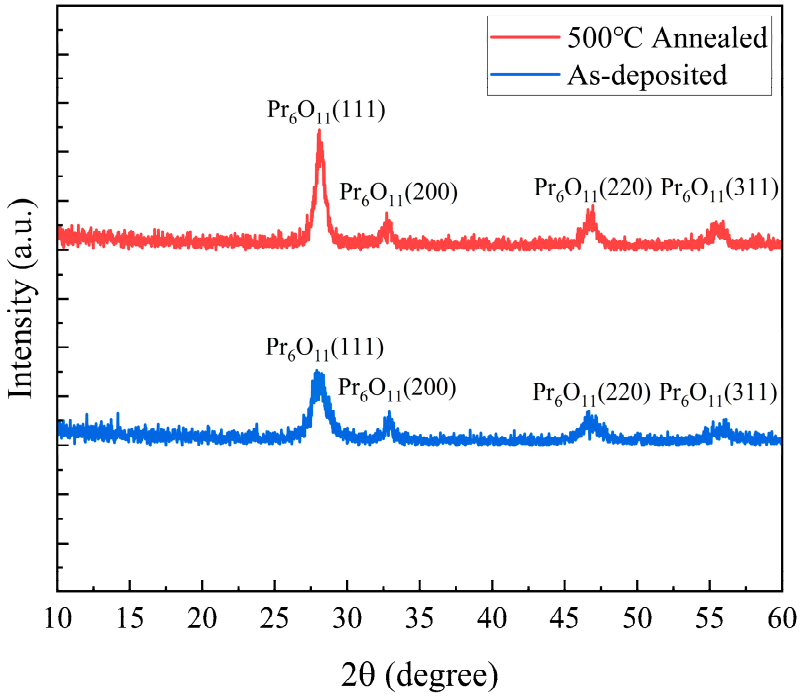

Figure 6. Crystal structure of PrO_x thin films measured by XRD.

XPS was used to investigate the composition ratio of Pr^{3+} and Pr^{4+} in both the as-deposited sample and the sample annealed at 500 °C [54]. As shown in Figure 7, deconvolution was performed on the Pr 3d spectrum to separate the superimposed peaks associated with various oxidation states (Pr^{3+}, Pr^{4+}) and bonding states [55]. The results showed the coexistence of Pr^{3+} and Pr^{4+} in both Figure 7a,b. Additionally, the areas of the main peaks obtained through deconvolution were calculated to determine the chemical composition ratio of the two oxidation states, as summarized in Table 3. For the case annealed at 500 °C, the Pr^{4+} ratio was 76.64%, slightly higher than the 73.48% observed in the as-deposited sample. This shows a similar trend to the findings of L. Grima et al., where heat treatment in an oxidizing atmosphere at high temperatures resulted in a higher Pr^{4+} content [56]. Although the XPS analysis of annealed PrO_x film showed a slight increase in Pr^{4+} over as-deposited, Pr^{3+} was still present. The relative increase in Pr^{4+} content means that Pr^{4+} can be more readily reduced to Pr^{3+}, which improves the ability of oxygen to absorb and release [57]. However, the fact that the composition ratio of Pr^{3+} and Pr^{4+} is maintained even at the operating temperature of 500 °C suggests that the structure of the PrO_x catalyst remains stable under the operating conditions of LT-SOFCs.

Table 3. The chemical composition ratio of Pr^{3+} and Pr^{4+}.

Parameters	500 °C 1 h Annealed	As-Deposited
Pr^{3+}	23.36%	26.52%
Pr^{4+}	76.64%	73.48%

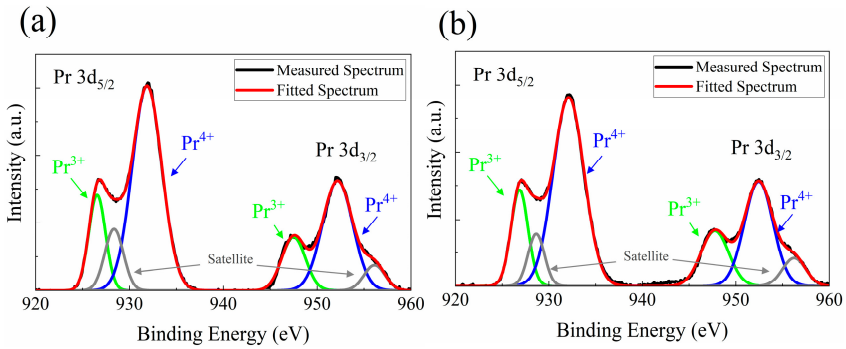

Figure 7. Pr 3d XPS spectra of PrO_x thin films (**a**) 500 °C 1 h annealed, (**b**) as-deposited.

The purpose of this study is to use PrO_x thin film as an interlayer for LT-SOFCs. Therefore, thermal stability was verified at the operating temperature of LT-SOFCs. Regarding the durability test, the severe agglomeration of porous Pt has difficulty in obtaining accurate measurements. Therefore, we analyzed the structural stability of the PrO_x cathode interlayer. As shown in Figure 8, after annealing 55 nm PrO_x thin films individually at 500 °C and 600 °C for 120 h and analyzing through SEM surface analysis, the films showed a stable microstructure without detecting cracks or particle growth. This stabilization will make the thin film structurally stable even in high-temperature environments during the operation of LT-SOFCs.

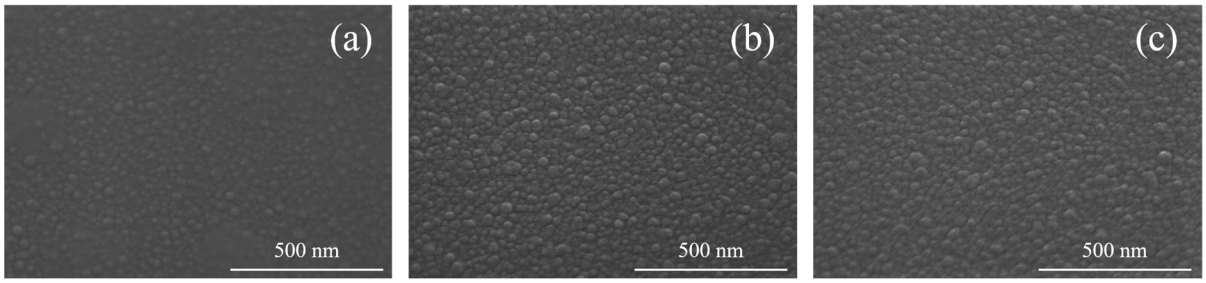

Figure 8. SEM surface images of PrO_x 55 nm films (**a**) as-deposited, (**b**) 500 °C annealed for 120 h, and (**c**) 600 °C annealed for 120 h.

3.2. Electrochemical Characteristics of LT-SOFCs Based on PrO_x Thickness

The electrochemical performance evaluation of LT-SOFCs with cathode interlayers of various thicknesses was conducted at 500 °C. For comparison, a case without a PrO_x cathode interlayer was also included. As shown in Figure 9, the OCV of all LT-SOFCs conditions was approximately 1.0 V. In the case of pure Pt without a cathode interlayer, the maximum power density reached 8.68 mW/cm^2. The Pr30 sample achieved 13.1 mW/cm^2, while the Pr55 sample showed a 26.5% improvement, reaching 17.9 mW/cm^2. However, the maximum power density of the Pr150 sample was 15.9 mW/cm^2, representing a 12.2% decrease compared to Pr55.

EIS was measured to analyze the electrochemical behavior of LT-SOFCs in greater detail. Ohmic resistance, which occurs when current flows through electrically conductive materials, corresponds to the x-intercept in the high-frequency region of the EIS graph shown in Figure 9a,b. The curve in the graph represents the faradaic resistance of the anode and cathode [1].

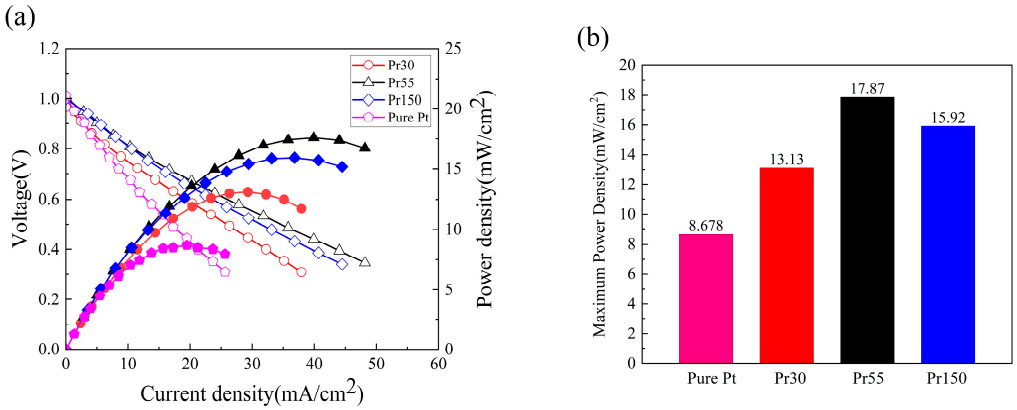

Figure 9. (**a**) j-V-P curves and (**b**) maximum power density. The solid shapes in the graph represent maximum power density, whereas the open shapes indicate current density.

Figure 10 presents the EIS results at 0.5 V for LT-SOFCs with PrO_x cathode interlayers of various thicknesses. The equivalent circuit was composed of a resistor (R), a constant phase element (Q), and Warburg impedance (W) to identify resistances [1,58]. R_1 represents the ohmic resistance, which is the electrical resistance of the electrolyte and electrode material itself. The parallel circuit consisting of R_2 and Q_2 represents the polarization resistance occurring at the anode. This corresponds to the hydrogen oxidation reaction occurring at the anode. The parallel circuit composed of R_3 and Q_3 represents the faradaic resistance at the cathode. For Pr30, the ohmic resistance and faradaic resistance were 5.42 Ω·cm^2 and 3.05 Ω·cm^2, respectively. Comparing the resistances of Pr30 with those of Pure Pt (Ohmic: 5.07 Ω·cm^2, Faradaic: 13.5 Ω·cm^2), the ohmic resistance showed a 6.37% increase, while the faradaic resistance decreased by approximately 3.4 times. This reduction of faradaic resistance leads to improved ORR performance, indicating an enhancement in the electrochemical reaction rate at the electrode. As in the preceding by Yuan Li et al., Pr_6O_{11} was applied to LSFM electrodes in a filtration method to significantly improve the electrode performance of LT-SOFCs by increasing the catalytic activity of the electrode and reducing the faradaic resistance [59]. Compared to previous studies, the PrO_x cathode interlayer would have promoted the ORR kinetics in this study.

The ohmic resistance and faradaic resistance of Pr55 were measured as 6.12 Ω·cm^2 and 2.57 Ω·cm^2, respectively, while those of Pr150 were measured as 6.74 Ω·cm^2 and 2.45 Ω·cm^2. It was observed that as the thickness of the PrO_x thin film increased, the ohmic resistance increased slightly, while the faradaic resistance decreased. Considering the Pr30 case, as the thickness of PrO_x increased, the ohmic resistance increased, while the faradaic resistance decreased. This increase in ohmic resistance is attributed to the longer ion conduction pathways through the thicker cathode interlayer. The TPB is the point where electrons, ions, and gases meet, serving as the primary location for electrochemical reactions [60,61]. Between the Pt cathode and the PrO_x interlayer, PrO_x serves as an ionic conductor, providing a pathway for oxygen ions generated at the Pt surface to transfer to the electrolyte. Additionally, it offers extra reaction sites around the Pt particles, increasing the region of TPBs. Furthermore, PrO_x acts as an MIEC, forming a Double Phase Boundary (DPB) [16,55]. DPB refers to a two-phase interface where gas and electrode meet. Unlike TPBs, where the reaction occurs only at a specific point where the three phases meet, an electrochemical reaction occurs throughout the surface of the material. This can provide more active sites and significantly improve electrochemical performance. Within PrO_x layer, oxygen vacancies and the redox transitions between Pr^{3+} and Pr^{4+} facilitate the generation and transformation of oxygen intermediates (O^{2-}, O*), enabling easier oxygen ion transport [4,40]. As the thickness of PrO_x increases, the number of oxygen vacancies in

the PrO_x layer increases. Not only can this store and release oxygen, but it can also provide more pathways for oxygen ions to move. In other words, it can provide more oxygen storage capacity overall, promoting oxygen ion transport and expanding the active reaction zone. The decrease in faradaic resistance is attributed to the presence of these additional active sites. Similar to the findings of the previous study of Park et al., the application of a GDC interlayer resulted in an increase in ohmic resistance but a significant reduction in faradaic resistance due to improved ionic conductivity, demonstrating a comparable trend [62]. This is because the relatively thicker cathode interlayer promotes the ORR reaction to reduce faradaic resistance, thereby improving electrochemical performance [59]. However, the performance degradation due to ohmic resistance due to an increase in thickness should also be considered.

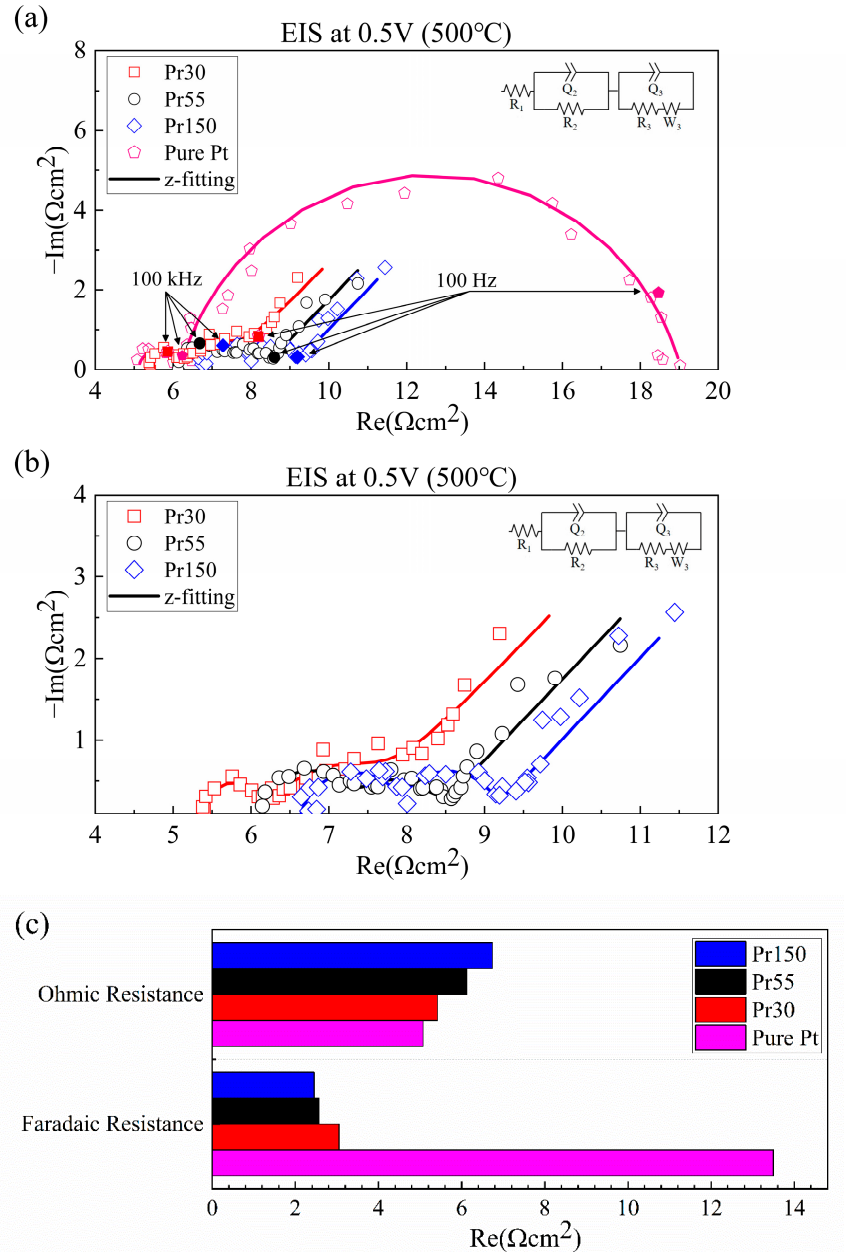

Figure 10. (**a**) EIS curves at 0.5 V, (**b**) EIS curves at 0.5 V without pure Pt, (**c**) magnitude of ohmic and Faradaic resistance.

From Pr30 to Pr150, as shown in Table 4, we observe an increase in Q_3 values as the PrO_x cathode interlayer is added or increased. PrO_x, with its high oxygen defect

concentration, facilitates oxygen ion storage and transport. The increased Q_3 indicates enhanced charge storage capacity of the cathode surface, suggesting improved ORR due to the increased active sites of PrO_x [63,64]. Previous research by L. Navarrete et al. demonstrated that Pr infiltration enhances oxygen dissociation and adsorption processes, leading to improved ORR [65]. Conversely, the R_3 value decreases with the PrO_x cathode interlayer, indicating more efficient ORR and improved oxygen ion conductivity due to increased oxygen vacancies. In EIS analysis, the 100 kHz–100 Hz range corresponds to electrochemical reactions at the cathode. R. K. Sharma et al. observed that the oxygen reduction reaction process is primarily detected in this range [64]. Additionally, the low-frequency range (f < 100 Hz) is associated with gas diffusion impedance. Hjelm et al. observed gas diffusion impedance at 120 Hz in an LSCF + CGO composite cathode, varying with oxygen partial pressure [66]. These findings collectively demonstrate the significant role of the PrO_x cathode interlayer in enhancing the electrochemical performance of SOFCs [67].

Table 4. R_3 and Q_3 values of LT-SOFCs.

Parameters	Pure Pt	Pr30	Pr55	Pr150
R_3 ($\Omega \cdot cm^2$)	16.4	2.42	1.43	1.39
Q_3 ($F \cdot s^{\alpha-1}$)	2.02×10^{-6}	2.83×10^{-6}	1.01×10^{-5}	1.53×10^{-5}

Meanwhile, in LT-SOFCs with a PrO_x cathode interlayer, Warburg impedance was commonly observed in the low-frequency region [68]. Warburg impedance appears as a straight line with a slope of 45 degrees in the low-frequency region and represents the resistance arising from the diffusion of oxygen ions generated by the ORR reaction within the PrO_x layer [1,58,69]. Since oxygen ions neither move nor diffuse within the cathode in the case of Pure Pt, Warburg impedance was not observed. However, when a PrO_x cathode interlayer was applied, its excellent oxygen exchange capability rapidly facilitated the ORR reaction. Warburg impedance was observed because the diffusion path of oxygen molecules within the cathode has a finite length. Notably, PrO_x has an oxygen-excess structure, which contributes to high oxygen ion conductivity but simultaneously forms an oxygen concentration gradient within the electrode, affecting the Warburg impedance [16]. In fact, according to a previous study, Warburg impedance was observed in the oxygen gas diffusion process due to the oxygen-excess structure of $Pr_2NiO_{4+\delta}$ [67,70].

3.3. Evaluation of LT-SOFC with PrO_x Cathode Interlayer Based on Thermal Dependence

In this study, Pt cathode was used as the reference cell due to its excellent catalytic activity and outstanding electronic conductivity. Meanwhile, Lanthanum strontium cobaltite ($La_{0.6}Sr_{0.4}CoO_{3-x}$, LSC) is a Mixed Ionic-Electronic Conductor (MIEC) that simultaneously transfers electrons and oxygen and is widely used as a cathode material for SOFCs [71,72]. In this research, LSC was added as another cathode material to compare the thermal dependence of Low-Temperature Solid Oxide Fuel Cells (LT-SOFCs). LT-SOFCs with LSC cathodes of the same thickness (150 nm) were fabricated. The anode and electrolyte are identical to those in the Pure Pt case and cases with PrO_x cathode interlayer applied. LSC was produced through sputtering under process conditions of 15 mTorr pressure, 30 sccm Ar flow rate, and 40 W power. The operating environment remains the same as before, but a temperature condition of 600 °C was added to investigate the electrochemical characteristics according to temperature.

As shown in Figure 11, The measurement results showed that at 500 °C, LSC exhibited a maximum power density of 5.41 mW/cm^2, which is 37.6% lower than that of Pure Pt (8.68 mW/cm^2). Additionally, at 600 °C, Pure Pt showed 33.8 mW/cm^2, while LSC showed 24.8 mW/cm^2. Additionally, the electrochemical performance of Pr55, which exhibited

the highest maximum power density at 500 °C, was measured at 600 °C under the same conditions as the 500 °C test. The maximum power density of Pr55 at 600 °C was measured as 62.36 mW/cm^2, representing a significant improvement of 3.48 times compared to 500 °C.

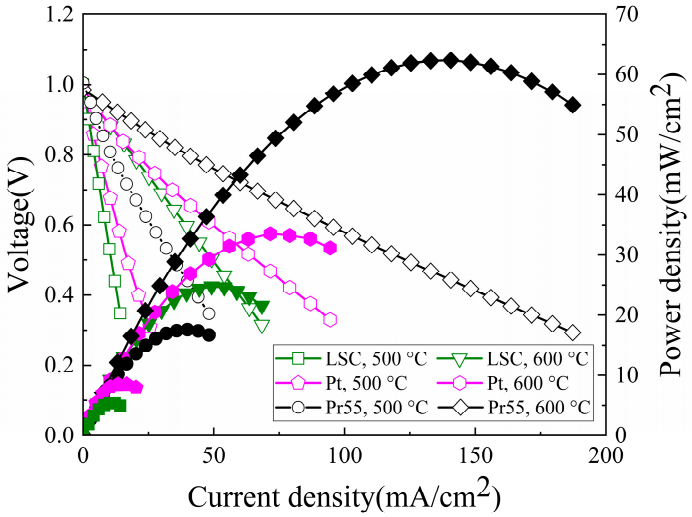

Figure 11. j-V-P curves of LSC cathode and Pt cathode at 500 °C and 600 °C. The solid shapes in the graph represent maximum power density, whereas the open shapes indicate current density.

As shown in the EIS spectra (Figure 12), the ohmic resistance of LSC at 500 °C was confirmed to be 21.0 Ω·cm^2. This exhibited a much higher ohmic resistance compared to Pure Pt (5.07 Ω·cm^2). This is because the electronic conductivity of LSC at 500 °C is much lower than that of metallic Pt, resulting in higher electrical resistance. A.A. Solovyev et al. reported that the electrical conductivity of pure LSC cathode significantly decreases at an operating temperature of 500 °C [73]. On the other hand, the faradaic resistance was 10.9 Ω·cm^2, which is 19.3% lower than Pt's 13.5 Ω·cm^2. LSC, being an MIEC, forms DPB, providing more active sites and thus improving electrochemical reactions. Similarly, at 600 °C, the ohmic resistance and faradaic resistance of Pt cathode and LSC cathode showed the same trend. The ohmic resistance of LSC was 11.1 Ω·cm^2, about 8 times larger than Pure Pt's 1.38 Ω·cm^2. Additionally, the faradaic resistance for LSC and Pt cathode was 4.03 Ω·cm^2 and 4.97 Ω·cm^2, respectively. As with 500 °C, this indicates that while LSC has a higher ohmic resistance than Pt due to lower electronic conductivity, its faradaic resistance decreases as an MIEC by expanding reaction sites.

The ohmic resistance of Pr55 at 600 Ω·cm^2 was measured as 1.524 Ω·cm^2, and the Faradaic resistance as 0.771 Ω·cm^2. This improvement is due to the enhanced electronic conductivity of the Pt electrode and the PrO_x layer as the temperature increased, leading to a significant reduction in ohmic resistance [74]. Furthermore, the catalytic activity was greatly improved with the increase in temperature, which significantly promoted the ORR [16,35]. As a result, the Faradaic resistance was reduced.

For further analysis of the PrO_x Cathode Interlayer, exchange current densities were calculated from j-V-P curves and plotted as a Tafel plot [1,74]. The exchange current density is a parameter that expresses the rate of oxidation and reduction reactions occurring on the electrode surface as a current density when the electrode is in equilibrium [75]. As shown in Figure 13, Pure Pt exhibited an exchange current density of 2.23 mA/cm^2, while Pr30 showed 4.74 mA/cm^2, Pr55 displayed 5.98 mA/cm^2, and Pr150 demonstrated 6.10 mA/cm^2. Lastly, LSC exhibited an exchange current density of 1.98 mA/cm^2. LSC cathode showed the lowest j_0 among the results mentioned above. This is attributed to the relatively low electrical conductivity and catalytic activity at 500 °C. On the other hand, all cases with applied PrO_x cathode interlayers displayed superior exchange current densities

compared to Pure Pt. This improvement can be attributed to the PrO_x layer enhancing the interface characteristics between the cathode and electrolyte, as well as improving reaction rates due to increased active sites. Furthermore, the mixed ionic conducting properties of PrO_x facilitated the expansion of active reaction sites on the electrode, resulting in enhanced overall performance [76].

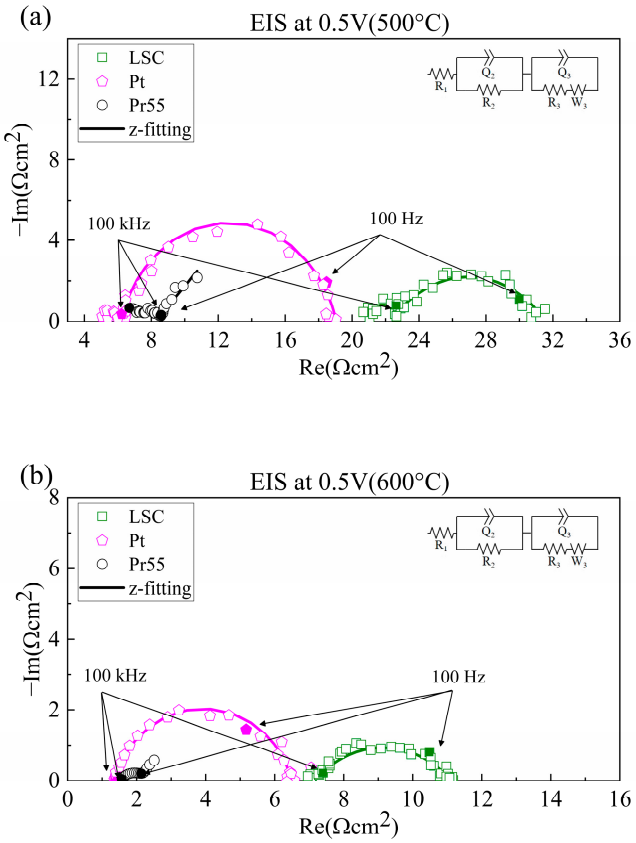

Figure 12. EIS results of LSC Pt cathode and Pr55 case at 0.5 V (**a**) 500 °C, (**b**) 600 °C.

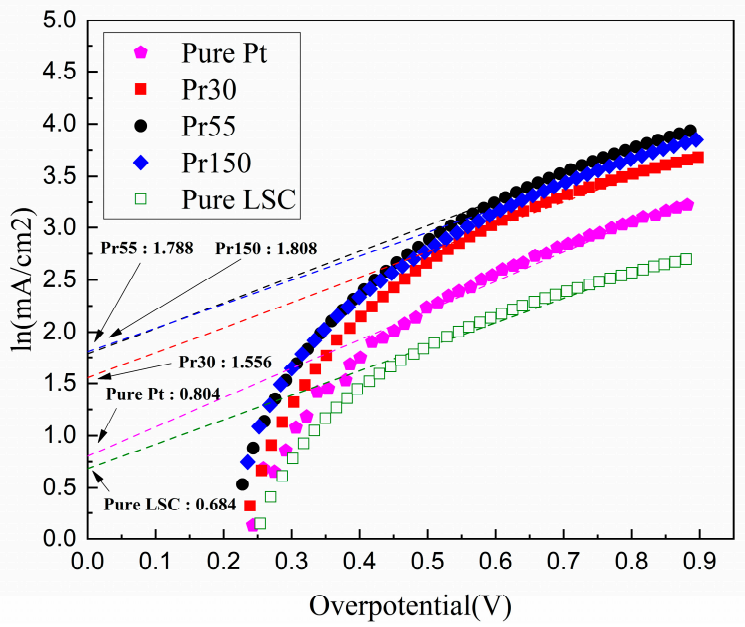

Figure 13. Tafel plot of LT-SOFCs at 500 °C.

Based on the j-V-P curves measured at 500 °C and 600 °C for Pt cathode, LSC cathode, and Pr55, calculated the exchange current density and, referring to relevant references, plotted an Arrhenius plot [77,78] in Figure 14. Additionally, we calculated the activation energy using the slope of the plot's straight line. The activation energy of the Pt cathode is 1.03 eV, the LSC cathode is 1.22 eV, and Pr55's activation energy is 0.82 eV. LSC, which showed the highest activation energy, despite being an MIEC capable of transferring both electrons and oxygen ions, resulted in a large activation energy due to its lower electrical conductivity compared to Pt at 500 °C. On the other hand, Pr55, which showed the lowest activation energy, can improve the catalytic properties of Pt and enhance oxygen ion conductivity as an MIEC by PrO_x [67,76].

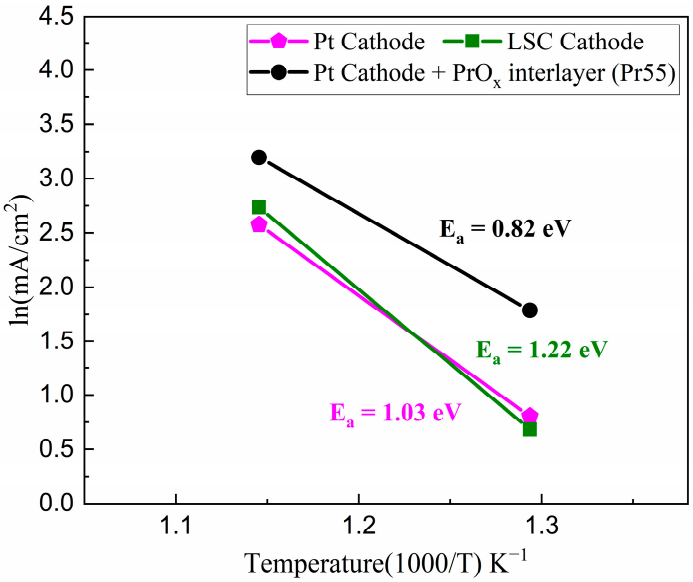

Figure 14. Arrhenius plot of LT-SOFCs.

4. Conclusions

Throughout this study, it was demonstrated that stable PrO_x thin films can be deposited via reactive sputtering. SEM analysis confirmed the microstructure of thin films. Considering the operating temperature of 500 °C for LT-SOFCs, the thin-film properties of PrO_x were analyzed using XRD, revealing improved crystallinity compared to the as-deposited state. XPS analysis showed a higher oxidation state (Pr^{4+}) at 500 °C. This higher oxidization state provides a higher oxygen storage capacity and can easily cause redox reactions through high reduction potential. Additionally, electrochemical performance evaluation was conducted on LT-SOFCs fabricated with ScSZ electrolytes based on this process condition. It was observed that the application of the PrO_x interlayer and the increase in interlayer thickness led to an increase in ohmic resistance. However, the increase of reaction sites for ORR increased, resulting in a significant reduction of faradaic resistance. In conclusion, the application of the PrO_x cathode interlayer effectively enhanced the performance of LT-SOFCs.

Author Contributions: Conceptualization, J.-W.J.; methodology, J.-W.J.; validation, J.-G.P.; formal analysis, J.-W.J.; investigation, J.-W.J.; resources, J.-G.P. and G.-H.K.; data curation, S.-H.L.; writing—original draft, J.-W.J.; writing—review and editing, J.-W.S. and G.-Y.C.; visualization, J.-W.J.; supervision, J.-W.S. and G.-Y.C. All authors have read and agreed to the published version of the manuscript.

Funding: This work was supported by the Korea Institute of Energy Technology Evaluation and Planning (KETEP) grant funded by the Korean government (MOTIE) (20213030030260). This work

was supported by the National Research Foundation of Korea (NRF) grant funded by the Korean government (MSIT). (No. RS-2023-00213741). This work was supported by the Technology Innovation Program (20025646) funded by the Ministry of Trade, Industry & Energy (MOTIE, Korea).

Institutional Review Board Statement: Not applicable.

Informed Consent Statement: Not applicable.

Data Availability Statement: The data presented in this study are available on request from the corresponding author.

Conflicts of Interest: The authors declare no conflicts of interest.

References

1. O'Hayre, R.; Cha, S.-K.; Colella, W.; Prinz, F.B. *Fuel Cell Fundamentals*, 3rd ed.; Wiley: Hoboken, NJ, USA, 2016.
2. Sharaf, O.Z.; Orhan, M.F. An overview of fuel cell technology: Fundamentals and applications. *Renew. Sustain. Energy Rev.* **2014**, *32*, 810–853. [CrossRef]
3. Liu, M.; Lynch, M.E.; Blinn, K.; Alamgir, F.M.; Choi, Y. Rational SOFC material design: New advances and tools. *Mater. Today* **2011**, *14*, 534–546. [CrossRef]
4. Cho, G.Y.; Lee, Y.H.; Cha, S.W. Multi-component nano-composite electrode for SOFCS via thin film technique. *Renew. Energy* **2014**, *65*, 130–136. [CrossRef]
5. Ivers-Tiffée, E.; Weber, A.; Herbstritt, D. Materials and technologies for SOFC-components. *J. Eur. Ceram. Soc.* **2001**, *21*, 1805–1811. [CrossRef]
6. Kaur, P.; Singh, K. Review of perovskite-structure related cathode materials for solid oxide fuel cells. *Ceram. Int.* **2020**, *46*, 5521–5535. [CrossRef]
7. El Haj Assad, M.; Khosravi, A.; Hashemian, M. The Fundamentals of Thermal Analysis. *Nova Sci. Publ.* **2023**. [CrossRef]
8. Yoda, M.; Inoue, S.; Takuwa, Y.; Yasuhara, K.; Suzuki, M. Development and Commercialization of New Residential SOFC CHP System. *ECS Trans.* **2017**, *78*, 125–132. [CrossRef]
9. Wachsman, E.D.; Lee, K.T. Lowering the temperature of solid oxide fuel cells. *Science* **2011**, *334*, 935–939. [CrossRef] [PubMed]
10. Mahato, N.; Banerjee, A.; Gupta, A.; Omar, S.; Balani, K. Progress in material selection for solid oxide fuel cell technology: A review. *Prog. Mater. Sci.* **2015**, *72*, 141–337. [CrossRef]
11. Sun, C.; Hui, R.; Roller, J. Cathode materials for solid oxide fuel cells: A review. *J. Solid State Electrochem.* **2010**, *14*, 1125–1144. [CrossRef]
12. González-García, K.; Montemayor, S.; la Rosa, G.M.-D.; Durá, O.; Bazaldúa-Medellín, M.; Burciaga-Díaz, O.; Díaz-Guillén, J. Electrical and thermal properties of LT-SOFC solid electrolytes: Sm cerates/zirconates obtained by mechanochemistry. *Int. J. Hydrogen Energy* **2024**, *in press*. [CrossRef]
13. Guo, X.; Guo, Y.; Wang, J.; Meng, X.; Deng, B.; Wu, W.; Zhao, P. Thermodynamic analysis of a novel combined heating and power system based on low temperature solid oxide fuel cell (LT-SOFC) and high temperature proton exchange membrane fuel cell (HT-PEMFC). *Energy* **2023**, *284*, 129227. [CrossRef]
14. Patakangas, J.; Ma, Y.; Jing, Y.; Lund, P. Review and analysis of characterization methods and ionic conductivities for low-temperature solid oxide fuel cells (LT-SOFC). *J. Power Sources* **2014**, *263*, 315–331. [CrossRef]
15. dos Santos-Gómez, L.; Zamudio-García, J.; Porras-Vázquez, J.M.; Losilla, E.R.; Marrero-López, D. Recent progress in nanostructured electrodes for solid oxide fuel cells deposited by spray pyrolysis. *J. Power Sources* **2021**, *507*, 230277. [CrossRef]
16. Nicollet, C.; Flura, A.; Vibhu, V.; Rougier, A.; Bassat, J.-M.; Grenier, J.-C. An innovative efficient oxygen electrode for SOFC: Pr 6 O 11 infiltrated into Gd-doped ceria backbone. *Int. J. Hydrogen Energy* **2016**, *41*, 15538–15544. [CrossRef]
17. Hong, S.; Oh, S.; Kim, H.J.; Lim, Y.; An, J.; Kim, Y.-B. Enhanced Thermal Stability of a Gadolinia-Doped Ceria Capped Metal Electrode for Durable Low-Temperature Solid Oxide Fuel Cells. *J. Electrochem. Soc.* **2017**, *164*, F1301–F1306. [CrossRef]
18. Yang, B.C.; Go, D.; Oh, S.; Shin, J.W.; Kim, H.J.; An, J. Atomic-layer-deposited ZrO_2-doped CeO_2 thin film for facilitating oxygen reduction reaction in solid oxide fuel cell. *Appl. Surf. Sci.* **2019**, *473*, 102–106. [CrossRef]
19. Kim, Y.B.; Shim, J.H.; Gür, T.M.; Prinz, F.B. Epitaxial and Polycrystalline Gadolinia-Doped Ceria Cathode Interlayers for Low Temperature Solid Oxide Fuel Cells. *J. Electrochem. Soc.* **2011**, *158*, B1453–B1457. [CrossRef]
20. Bae, J.; Hong, S.; Koo, B.; An, J.; Prinz, F.B.; Kim, Y.-B. Influence of the grain size of samaria-doped ceria cathodic interlayer for enhanced surface oxygen kinetics of low-temperature solid oxide fuel cell. *J. Eur. Ceram. Soc.* **2014**, *34*, 3763–3768. [CrossRef]
21. Jeong, W.; Yu, W.; Lee, M.S.; Bai, S.J.; Cho, G.Y.; Cha, S.W. Ultrathin sputtered platinum–gadolinium doped ceria cathodic interlayer for enhanced performance of low temperature solid oxide fuel cells. *Int. J. Hydrogen Energy* **2020**, *45*, 32442–32448. [CrossRef]

22. Develos-Bagarinao, K.; Budiman, R.A.; Liu, S.-S.; Ishiyama, T.; Kishimoto, H.; Yamaji, K. Evolution of cathode-interlayer interfaces and its effect on long-term degradation. *J. Power Sources* **2020**, *453*, 227894. [CrossRef]
23. Chrzan, A.; Karczewski, J.; Szymczewska, D.; Jasinski, P. Nanocrystalline cathode functional layer for SOFC. *Electrochim. Acta* **2017**, *225*, 168–174. [CrossRef]
24. Lee, Y.H.; Ren, H.; Wu, E.A.; Fullerton, E.E.; Meng, Y.S.; Minh, N.Q. All-Sputtered, Superior Power Density Thin-Film Solid Oxide Fuel Cells with a Novel Nanofibrous Ceramic Cathode. *Nano Lett.* **2020**, *20*, 2943–2949. [CrossRef] [PubMed]
25. Develos-Bagarinao, K.; Ishiyama, T.; Kishimoto, H.; Shimada, H.; Yamaji, K. Nanoengineering of cathode layers for solid oxide fuel cells to achieve superior power densities. *Nat. Commun.* **2021**, *12*, 3979. [CrossRef]
26. Nicollet, C.; Waxin, J.; Dupeyron, T.; Flura, A.; Heintz, J.-M.; Ouweltjes, J.P.; Piccardo, P.; Rougier, A.; Grenier, J.-C.; Bassat, J.-M. Gadolinium doped ceria interlayers for Solid Oxide Fuel Cells cathodes: Enhanced reactivity with sintering aids (Li, Cu, Zn), and improved densification by infiltration. *J. Power Sources* **2017**, *372*, 157–165. [CrossRef]
27. Sumi, H.; Takahashi, S.; Yamaguchi, Y.; Shimada, H. Lanthanum-doped ceria interlayer between electrolyte and cathode for solid oxide fuel cells. *J. Asian Ceram. Soc.* **2021**, *9*, 609–616. [CrossRef]
28. Sun, J.L.; Wang, J.X.; He, C.R.; Shen, P.; Wang, Q.; Miao, H.; Wang, W.G. Synthesis and electrical properties of screen-printed doped ceria interlayer for IT-SOFC applications. *J. Alloys Compd.* **2015**, *628*, 450–457. [CrossRef]
29. Matović, B.; Pantić, J.; Prekajski, M.; Stanković, N.; Bučevac, D.; Minović, T.; Čebela, M. Synthesis and characterization of Pr_6O_{11} nanopowders. *Ceram. Int.* **2013**, *39*, 3151–3155. [CrossRef]
30. Yi, Y.; Xi, X.; Huang, L.; Liu, X.; Liao, Y.; Liu, J.; Long, J.; Zhang, J.; Fu, X.; Luo, J. Boosting the Performance and Stability of Perovskites by Construction of NiFe Alloy and PrO_x Heterogeneously Structured Composites for High-Performance Solid Oxide Fuel Cell Anode. *Adv. Funct. Mater.* **2024**, *35*, 2412486. [CrossRef]
31. Thangadurai, V.; Huggins, R.A.; Weppner, W. Mixed ionic-electronic conductivity in phases in the praseodymium oxide system. *J. Solid State Electrochem.* **2001**, *5*, 531–537. [CrossRef]
32. Frizon, V.; Bassat, J.-M.; Pollet, M.F.; Durand, E.; Hernandez, J.; Pajot, K.; Vernoux, P.; Demourgues, A. Tuning the Pr Valence State to Design High Oxygen Mobility, Redox and Transport Properties in the CeO_2–ZrO_2–PrO_x Phase Diagram. *J. Phys. Chem. C* **2019**, *123*, 6351–6362. [CrossRef]
33. Corby, S.; Francàs, L.; Kafizas, A.; Durrant, J.R. Determining the role of oxygen vacancies in the photoelectrocatalytic performance of WO_3 for water oxidation. *Chem. Sci.* **2020**, *11*, 2907–2914. [CrossRef] [PubMed]
34. Lu, M.Y.; Scipioni, R.; Park, B.-K.; Yang, T.; Chart, Y.A.; Barnett, S.A. Mechanisms of PrO_x performance enhancement of oxygen electrodes for low and intermediate temperature solid oxide fuel cells. *Mater. Today Energy* **2019**, *14*, 100362. [CrossRef]
35. Okada, S.; Miyoshi, S.; Yamaguchi, S. Rate Determining Step in ORR of PrO_x-Based Film Cathodes. *ECS Trans.* **2015**, *68*, 987–994. [CrossRef]
36. Naiqing, Z.; Kening, S.; Derui, Z.; Dechang, J. Study on Properties of LSGM Electrolyte Made by Tape Casting Method and Applications in SOFC. *J. Rare Earths* **2006**, *24*, 90–92. [CrossRef]
37. Moon, H.; Kim, S.D.; Hyun, S.H.; Kim, H.S. Development of IT-SOFC unit cells with anode-supported thin electrolytes via tape casting and co-firing. *Int. J. Hydrogen Energy* **2008**, *33*, 1758–1768. [CrossRef]
38. Lee, H.; Park, J.; Lim, Y.; Yang, H.; Kim, Y.-B. Flash light sintered SDC cathodic interlayer for enhanced oxygen reduction reaction in LT-SOFCs. *J. Alloys Compd.* **2021**, *861*, 158397. [CrossRef]
39. Dubal, S.; Jamale, A.; Jadhav, S.; Patil, S.; Bhosale, C.; Jadhav, L. Yttrium doped $BaCeO_3$ thin films by spray pyrolysis technique for application in solid oxide fuel cell. *J. Alloys Compd.* **2014**, *587*, 664–669. [CrossRef]
40. Choi, S.; Yoo, S.; Shin, J.-Y.; Kim, G. High Performance SOFC Cathode Prepared by Infiltration of $La_{n+1}Ni_nO_{3n+1}$ (n = 1, 2, and 3) in Porous YSZ. *J. Electrochem. Soc.* **2011**, *158*, B995–B999. [CrossRef]
41. Yu, W.; Lee, S.; Jeong, W.; Cho, G.Y.; Lee, Y.H.; Cha, S.W. High performance, enhanced structural stability of co-sputtered nanocomposite anode with neutral stress state for low-temperature solid oxide fuel cells. *Mater. Today Energy* **2023**, *34*, 101308. [CrossRef]
42. Pan, Y.; Wang, J.; Lu, Z.; Wang, R.; Xu, Z. A review on the application of magnetron sputtering technologies for solid oxide fuel cell in reduction of the operating temperature. *Int. J. Hydrogen Energy* **2024**, *50*, 1179–1193. [CrossRef]
43. Yang, Y.; Zhang, Y.; Yan, M. A review on the preparation of thin-film YSZ electrolyte of SOFCs by magnetron sputtering technology. *Sep. Purif. Technol.* **2022**, *298*, 121627. [CrossRef]
44. Pan, T.-M.; Hsieh, C.-I.; Tsai, F.-J.; Wu, T.-W. Excellent Electrical Characteristics of Praseodymium Oxide Dielectrics on Si Substrate by Reactive RF Sputtering. *ECS Trans.* **2007**, *6*, 247–250. [CrossRef]
45. Lakshmi, V.V.; Bauri, R.; Gandhi, A.S.; Paul, S. Synthesis and characterization of nanocrystalline ScSZ electrolyte for SOFCs. *Int. J. Hydrogen Energy* **2011**, *36*, 14936–14942. [CrossRef]
46. Thomas, J.H. Effect of pressure on dc planar magnetron sputtering of platinum. *J. Vac. Sci. Technol. A Vac. Surf. Films* **2003**, *21*, 572–576. [CrossRef]

47. Kang, S.; Su, P.C.; Park, Y.I.; Saito, Y.; Prinz, F.B. Thin-Film Solid Oxide Fuel Cells on Porous Nickel Substrates with Multistage Nanohole Array. *J. Electrochem. Soc.* **2006**, *153*, A554–A559. [CrossRef]
48. Wang, W.; Su, C.; Wu, Y.; Ran, R.; Shao, Z. Progress in solid oxide fuel cells with nickel-based anodes operating on methane and related fuels. *Chem. Rev.* **2013**, *113*, 8104–8151. [CrossRef] [PubMed]
49. Liang, H.; Xu, J.; Zhou, D.; Sun, X.; Chu, S.; Bai, Y. Thickness dependent microstructural and electrical properties of TiN thin films prepared by DC reactive magnetron sputtering. *Ceram. Int.* **2016**, *42*, 2642–2647. [CrossRef]
50. Zhang, L.; Yang, H.; Pang, X.; Gao, K.; Volinsky, A.A. Microstructure, residual stress, and fracture of sputtered TiN films. *Surf. Coat. Technol.* **2013**, *224*, 120–125. [CrossRef]
51. Chen, D.; Bishop, S.R.; Tuller, H.L. Praseodymium-cerium oxide thin film cathodes: Study of oxygen reduction reaction kinetics. *J. Electroceramics* **2012**, *28*, 62–69. [CrossRef]
52. Faryna, M.; Adamczyk-Habrajska, M.; Lubszczyk, M. Influence of grain boundary plane distribution on ionic conductivity in yttria-stabilized zirconia sintered at elevated temperatures. *Arch. Civ. Mech. Eng.* **2024**, *24*, 123. [CrossRef]
53. Korte, C.; Peters, A.; Janek, J.; Hesse, D.; Zakharov, N. Ionic conductivity and activation energy for oxygen ion transport in superlattices—The semicoherent multilayer system YSZ (ZrO_2 + 9.5 mol% Y_2O_3)/Y_2O_3. *Phys. Chem. Chem. Phys.* **2008**, *10*, 4623–4635. [CrossRef] [PubMed]
54. Zhang, W.; Shiraiwa, M.; Wang, N.; Ma, T.; Fujii, K.; Niwa, E.; Yashima, M. Pr/Ba cation-disordered perovskite $Pr_{2/3}Ba_{1/3}CoO_{3-\delta}$ as a new bifunctional electrocatalyst for oxygen reduction and oxygen evolution reactions. *J. Ceram. Soc. Jpn.* **2018**, *126*, 814–819. [CrossRef]
55. Kamecki, B.; Miruszewski, T.; Karczewski, J. Structural and electrical transport properties of Pr-doped $SrTi_{0.93}Co_{0.07}O_{3-\delta}$ a novel SOEC fuel electrode materials. *J. Electroceramics* **2019**, *42*, 31–40. [CrossRef]
56. Grima, L.; Peña, J.; Sanjuán, M. Pyrochlore-like ZrO_2-PrO_x compounds: The role of the processing atmosphere in the stoichiometry, microstructure and oxidation state. *J. Alloys Compd.* **2022**, *923*, 166449. [CrossRef]
57. Poggio-Fraccari, E.; Baronetti, G.; Mariño, F. Pr^{3+} surface fraction in CePr mixed oxides determined by XPS analysis. *J. Electron Spectrosc. Relat. Phenom.* **2018**, *222*, 1–4. [CrossRef]
58. Lazanas, A.C.; Prodromidis, M.I. Electrochemical Impedance Spectroscopy—A Tutorial. *ACS Meas. Sci. Au* **2023**, *3*, 162–193. [CrossRef] [PubMed]
59. Li, Y.; Tian, Y.; Li, Z.; Wu, X.; Wang, L.; Bian, T. Boosting the performance of $La_{0.5}Sr_{0.5}Fe_{0.9}Mo_{0.1}O_{3-\delta}$ oxygen electrode via surface-decoration with Pr_6O_{11} nano-catalysts. *Int. J. Hydrogen Energy* **2024**, *84*, 305–312. [CrossRef]
60. Timurkutluk, B.; Altan, T.; Toros, S.; Genc, O.; Celik, S.; Korkmaz, H.G. Engineering solid oxide fuel cell electrode microstructure by a micro-modeling tool based on estimation of TPB length. *Int. J. Hydrogen Energy* **2021**, *46*, 13298–13317. [CrossRef]
61. Li, Y.; Wang, S.; Su, P.-C. Proton-conducting Micro-solid Oxide Fuel Cells with Improved Cathode Reactions by a Nanoscale Thin Film Gadolinium-doped Ceria Interlayer. *Sci. Rep.* **2016**, *6*, 22369. [CrossRef]
62. Park, T.; Lee, Y.H.; Cho, G.Y.; Ji, S.; Park, J.; Chang, I.; Cha, S.W. Effect of the thickness of sputtered gadolinia-doped ceria as a cathodic interlayer in solid oxide fuel cells. *Thin Solid Films* **2015**, *584*, 120–124. [CrossRef]
63. Kim, H.Y.; Lee, S.W.; Lee, S.H.; Lee, Y.; Yu, J.H.; Shin, T.H. Accelerating the electrochemical performance of solid oxide fuel cells using a Ce(Gd, Bi, Yb)$O_{2-\delta}$ diffusion barrier layer acting as an oxygen reservoir at high-current loading conditions. *J. Mater. Chem. A* **2025**, *13*, 3474. [CrossRef]
64. Sharma, R.K.; Djurado, E. An efficient hierarchical nanostructured Pr_6O_{11} electrode for solid oxide fuel cells. *J. Mater. Chem. A* **2018**, *6*, 10787–10802. [CrossRef]
65. Navarrete, L.; Solís, C.; Serra, J.M. Boosting the oxygen reduction reaction mechanisms in IT-SOFC cathodes by catalytic functionalization. *J. Mater. Chem. A* **2015**, *3*, 16440–16444. [CrossRef]
66. Hjelm, J.; So⁄gaard, M.; Wandel, M.; Menon, M.; Mogensen, M.; Hagen, A. Electrochemical Impedance Studies of SOFC Cathodes. *ECS Trans.* **2007**, *7*, 1261–1270. [CrossRef]
67. Flura, A.; Nicollet, C.; Fourcade, S.; Vibhu, V.; Rougier, A.; Bassat, J.-M.; Grenier, J.-C. Identification and modelling of the oxygen gas diffusion impedance in SOFC porous electrodes: Application to $Pr_2NiO_{4+\delta}$. *Electrochim. Acta* **2015**, *174*, 1030–1040. [CrossRef]
68. Nielsen, J.; Jacobsen, T.; Wandel, M. Impedance of porous IT-SOFC LSCF:CGO composite cathodes. *Electrochim. Acta* **2011**, *56*, 7963–7974. [CrossRef]
69. Chart, Y.A.; Lu, M.Y.; A Barnett, S. High-Performance Oxygen Electrodes for Low Temperature Solid Oxide Cells. *ECS Meet. Abstr.* **2019**, *MA2019-01*, 1713. [CrossRef]
70. Nielsen, J.; Hjelm, J. Impedance of SOFC electrodes: A review and a comprehensive case study on the impedance of LSM:YSZ cathodes. *Electrochim. Acta* **2014**, *115*, 31–45. [CrossRef]
71. Mehdi, A.M.; Hussain, A.; Song, R.H.; Lim, T.-H.; Kazmi, W.W.; Ishfaq, H.A.; Khan, M.Z.; Qamar, S.; Syed, M.W.; Mehran, M.T. Improving the durability of cobaltite cathode of solid oxide fuel cells—A review. *RSC Adv.* **2023**, *13*, 25029–25053. [CrossRef]
72. Yoon, J.; Cho, S.; Kim, J.-H.; Lee, J.H.; Bi, Z.; Serquis, A.; Zhang, X.; Manthiram, A.; Wang, H. Vertically aligned nanocomposite thin films as a cathode/electrolyte interface layer for thin-film solid oxide fuel cells. *Adv. Funct. Mater.* **2009**, *19*, 3868. [CrossRef]

73. Solovyev, A.; Kuterbekov, K.; Nurkenov, S.; Nygymanova, A.; Shipilova, A.; Smolyanskiy, E.; Rabotkin, S.; Ionov, I. Anode-supported solid oxide fuel cells with multilayer LSC/CGO/LSC cathode. *Fuel Cells* **2021**, *21*, 408–412. [CrossRef]
74. Cho, G.Y.; Yu, W.; Lee, Y.H.; Lee, Y.; Tanveer, W.H.; Kim, Y.; Lee, S.; Cha, S.W. Effects of Nanoscale PEALD YSZ Interlayer for AAO Based Thin Film Solid Oxide Fuel Cells. *Int. J. Precis. Eng. Manuf.-Green Technol.* **2020**, *7*, 423–430. [CrossRef]
75. Yefsah, L. Study of the Reaction Mechanisms and Durability of Innovative Oxygen Electrode Materials for High Temperature Electrolysis. Ph.D. Thesis, Chemical Engineering, Université Grenoble Alpes, Grenoble, France, 2024.
76. Giuliano, A.; Nicollet, C.; Fourcade, S.; Mauvy, F.; Carpanese, M.P.; Grenier, J.-C. Influence of the electrode/electrolyte interface structure on the performance of $Pr_{0.8}Sr_{0.2}Fe_{0.7}Ni_{0.3}O_{3-\delta}$ as Solid Oxide Fuel Cell cathode. *Electrochim. Acta* **2017**, *236*, 328–336. [CrossRef]
77. Subardi, A.; Liao, K.-Y.; Fu, Y.-P. Oxygen permeation, thermal expansion behavior and electrochemical properties of $LaBa_{0.5}Sr_{0.5}Co_2O_{5+\delta}$ cathode for SOFCs. *RSC Adv.* **2017**, *7*, 14487–14495. [CrossRef]
78. Zhang, X.; Wang, L.; Espinoza, M.; Li, T.; Andersson, M. Numerical simulation of solid oxide fuel cells comparing different electrochemical kinetics. *Int. J. Energy Res.* **2021**, *45*, 12980–12995. [CrossRef]